

# The structure of cosmic voids in a $\Lambda$ CDM Universe

E. Ricciardelli<sup>1\*</sup>, V. Quilis<sup>1</sup>, S. Planelles<sup>2,3</sup>

<sup>1</sup>*Departament d'Astronomia i Astrofísica, Universitat de València, c/ Dr. Moliner 50, E-46100 - Burjassot, Valencia, Spain*

<sup>2</sup>*Astronomy Unit, Department of Physics, University of Trieste, via Tiepolo 11, I-34131 Trieste, Italy*

<sup>3</sup>*INAF, Osservatorio Astronomico di Trieste, via Tiepolo 11, I-34131 Trieste, Italy*

Accepted ... Received ...; in original form ...

## ABSTRACT

Eulerian cosmological codes are especially suited to properly describe the low density regions. This property makes this class of codes excellent tools to study the formation and evolution of cosmic voids. Following such ideas, we present the results of an Eulerian adaptive mesh refinement (AMR) hydrodynamical and N-body simulation, that contrary to the common practice, has been designed to refine the computational grid in the underdense regions of the simulated volume. Thus, the void regions are better described due to the combined effect of the Eulerian character of the numerical technique and the use of high numerical resolution from the AMR approach. To analyse the outcome of this simulation, we have constructed a new void finder optimally suited to find the hierarchy of voids in AMR simulations. The algorithm identifies voids starting from the cells with least density and highest velocity divergence and then expanding the underdense volume until reaching the void walls, defined from the steepness of the density gradient. At redshift  $z = 0$ , in a cosmological box of comoving side length  $100 \text{ Mpc}/h$ , we identify hundreds of voids with sizes up to  $\sim 17 \text{ Mpc}/h$  and typical density contrast of  $-0.8$ , which show a complex morphology and an intricate hierarchy of nested structures. The analysis of their mass density profile leads to the conclusion that a universal density profile can be applied to voids of any size, density, morphology and redshift.

**Key words:** cosmology: dark matter – large-scale structure of Universe – methods: N-body simulations

## 1 INTRODUCTION

Large redshift surveys have shown that galaxies are distributed in a weblike configuration around large underdense regions, the so-called voids. The first large void, with a diameter of  $50 \text{ Mpc}/h$ , was identified by Kirshner et al. (1981) in the region of Bootes. Subsequent surveys have confirmed the existence of several voids (Vogeley et al. 1994; Shectman et al. 1996) that fill most of the volume of the Universe. However, voids have been difficult to study for a long time, as most of the spectroscopic surveys used to focus on the most clustered regions, where the majority of the galaxies lie. Only with the coming of large spectroscopic surveys as two-degree field galaxy survey (2dFGRS, Colless et al. 2001) and Sloan Digital Sky Survey (SDSS, York et al. 2000) the sample of voids has become large enough to allow statistical studies (Hoyle & Vogeley 2004; Croton et al. 2004; Patiri et al. 2006a; Hoyle et al. 2012; Pan et al. 2012).

In the framework of structure formation, voids are thought to form from negative density perturbations in the initial density field. In contrast to the overdense regions that turn around and collapse, these underdense regions evolve from the inside out. Linear theory predicts that as void expands the density in the interior continuously decreases, and matter accumulates at the boundaries, developing sharp edges. As a result of such an expansion, voids generate coherent outflows of matter and galaxies emptying the void volume (Padilla, Ceccarelli, & Lambas 2005; Ceccarelli et al. 2006; Patiri, Betancort-Rijo, & Prada 2012). Theoretically, the void evolution can be predicted by means of the excursion set formalism (Bond et al. 1991). Sheth & van de Weygaert (2004) showed that the void population can be described by requiring the random walks to cross two barriers, one referring to the critical density threshold involved with void merging (*void-in-void*) and the other to the disappearance of small voids embedded in large overdensities (*void-in-cloud*).

\* E-mail: elena.ricciardelli@uv.es

Besides being a striking feature of the cosmic web, voids

offer an excellent environment to probe cosmological models. The velocity outflows from the voids can be used to constrain  $\Omega_m$  (Dekel & Rees 1994), while their intrinsic structure and morphology is sensitive to the equation of state of dark energy (Park & Lee 2007; Lavaux & Wandelt 2010; Bos et al. 2012). Moreover, Lavaux & Wandelt (2012) have shown the potential use of the average shape of a stacked void to infer the cosmological parameters.

Another conspicuous feature is the existence of a void hierarchy, with small-scale voids embedded in the larger ones (van de Weygaert & van Kampen 1993; Sheth & van de Weygaert 2004; Aragon-Calvo & Szalay 2013). As voids expand, the fate of these substructures is the gradually fading of the small-scale underdensities in favor of the large surrounding void, though the void hierarchy never disappears completely.

In numerical simulations, one of the problems in the identification of voids is the definition of a void itself, as there is no clear consensus in literature on what is a genuine void (see Colberg et al. 2008 for a comparison of different void finders applied to numerical simulations). In the most simple case, voids can be defined as regions devoid of galaxies/haloes of a given luminosity/mass (Gottlöber et al. 2003; Patiri et al. 2006b), in the same way as done in galaxy redshift surveys (Varela et al. 2012; Pan et al. 2012; Hoyle et al. 2012). Void finders can also rely on the dark matter distribution (Plionis & Basilakos 2002; Colberg et al. 2005; Platen, van de Weygaert, & Jones 2007), identifying voids as underdense regions, using as a typical density contrast of  $-0.8$ , as suggested by the linear theory (Sheth & van de Weygaert 2004). In the majority of the void finders, voids are assumed to be spherical regions. Although simple arguments show that isolated voids will evolve into spherical voids (Icke 1984), the interaction with the surrounding environment is expected to let some imprints in the final structure of the void, with the result that voids become more elongated as time proceeds (Platen, van de Weygaert, & Jones 2008; Bos et al. 2012). Therefore, to capture the complexity of voids and of their substructures, more elaborate algorithms have been developed, such as the ZOBOV algorithm (Neyrinck 2008) and the watershed void finder (WVF, Platen, van de Weygaert, & Jones 2007, 2008; Aragon-Calvo & Szalay 2013), based on the tessellation technique. Here we introduce a new void finder that is optimally suited to find voids in AMR simulations. It shares with the WVF and ZOBOV procedures the capability of reconstructing the complex morphology of voids and of its nested hierarchy, although based on simpler arguments. In our definition, voids need to strictly satisfy some physical conditions, such as positive velocity divergence in the interior and sharp density gradients at the void boundaries. With these assumptions, we show how the algorithm is able to capture also the intricate web of substructures within voids.

The aim of the present work is to characterize the void population in a numerical simulation specifically designed to follow the formation and evolution of underdense regions. Void expansion is expected to stretch the small and medium-scale fluctuations located inside them (Aragon-Calvo & Szalay 2013; Neyrinck & Yang 2013), that

would be instead suppressed in overdense regions. As a consequence of such stretching, these small-scale fluctuations evolve forming a complex web of tenuous filaments and low-mass haloes. We have thus designed a refinement scheme that uses more resolution in voids, suitable to resolve such an intricate void substructure. With a new void finder devised for this task, we analyse the emerging void population, with a particular focus on the internal structure of voids.

The structure of the paper is the following. In Section 2 we describe the simulations used in this work. In Section 3 we detail the void finder algorithm and the tests done to verify its consistency. We present the results on the void population in Section 4 and conclude in Section 5.

## 2 THE SIMULATION

The simulation described in this paper is performed with the cosmological code MASCLET (Quilis 2004). This code couples an Eulerian approach based on high-resolution shock capturing techniques for describing the gaseous component, with a multigrid particle mesh N-body scheme for evolving the collisionless component (dark matter). Gas and dark matter are coupled by the gravity solver. Both schemes benefit of using an adaptive mesh refinement (AMR) strategy, which permits to gain spatial and temporal resolution.

The numerical simulation assumes a spatially flat  $\Lambda$ CDM cosmology, with the following cosmological parameters: matter density parameter,  $\Omega_m = 0.25$ ; cosmological constant,  $\Omega_\Lambda = \Lambda/3H_o^2 = 0.75$ ; baryon density parameter,  $\Omega_b = 0.045$ ; reduced Hubble constant,  $h = H_o/100 km s^{-1} Mpc^{-1} = 0.73$ ; power spectrum index,  $n_s = 1$ ; and power spectrum normalisation,  $\sigma_8 = 0.8$ .

The initial conditions are set up at  $z = 100$ , using a CDM transfer function from Eisenstein & Hu (1998), for a cube of comoving side length  $100 h^{-1} Mpc$ . The computational domain is discretised with  $512^3$  cubical cells.

A special set up is designed in order to produce a simulation specifically prepared to follow the formation and evolution of voids. Contrary to the common practice in cosmological simulations, where the regions with higher densities are best described, either by more particles in SPH technique due to their Lagrangian nature or by refined grids in AMR Eulerian schemes, we refine the coarse grids only in regions with low densities. To do so, we evolve the initial conditions until present time using Zel'dovich approximation. Those areas at the initial time,  $z = 100$ , which produce evolved regions with an overdensity,  $\rho/\rho_B$ , lower than 10 are refined, being  $\rho$  and  $\rho_B$  the total density and the background density, respectively. This value is a compromise between a correct coverage of the volume occupied by voids and the natural changes produced in the density contrast field during the evolution. If we consider that clusters follow a NFW profile ( $\rho/\rho_B \sim r^{-3}$ , Navarro, Frenk, & White 1997) out to their virial radius where the mean overdensity reaches values of 200, the use a threshold of 10 would give us a boundary zone around clusters of approximately two or three virial radii. In such a way, we ensure that our selection is focusing in the complementary part of galaxy clusters. Moreover, voids, and low density regions in general, evolve reducing their average density with time. A value as high as 10, also allows us to catch the early stages of voids and their boundaries.

Thus, the initial conditions are created on a coarse grid ( $256^3$  cells) with a first level of refinement (level  $l = 1$ ) on those regions which eventually would evolve to low density zones. The dark matter component in the initial refined regions is sampled with dark matter particles eight times lighter than those used in regions covered only by the coarse grid (level  $l = 0$ ).

The simulation presented in this paper uses a maximum of seven levels ( $l = 7$ ) of refinement, which gives a peak physical spatial resolution of  $\sim 3 h^{-1} kpc$  at  $z = 0$ . The ratio between the cell sizes for a given level ( $l+1$ ) and its parent level ( $l$ ) is, in our AMR implementation,  $\Delta x_{l+1}/\Delta x_l = 1/2$ . This is a compromise value between the gain in resolution and possible numerical instabilities. For the dark matter we consider two particles species, which correspond to the particles on the coarse grid and the particles within the first level of refinement at the initial conditions. The best mass resolution is  $\sim 5 \times 10^8 h^{-1} M_\odot$ , equivalent to distribute  $512^3$  particles in the whole box. Although we have only used levels up to  $l=1$  to analyse the voids in the present work, the formation and evolution of these regions depends on the description of the matter distribution on higher levels. On such levels, the gravity is numerically better resolved, and therefore, the dynamics is different.

During the evolution, we use a mixed strategy to both describe the voids and the denser regions within these voids. In a usual AMR simulation, we would refine a cell at the coarse level if its mass is larger than a given free simulation dependent mass threshold. Following this procedure, the cells at the newly created level of refinement would be refined when their masses would be larger than the same mass threshold, or equivalently, when the total density of the cells increase in a factor of eight compared with their parent cells. This procedure would be repeated at all levels of refinement. However, in the simulations used in this paper, the coarse grid is refined only in those regions where the overdensity is  $\rho/\rho_B \leq 10$ . To create the next level ( $l = 2$ ) of refinement, we used the standard approach, that is, the cells at  $l = 1$  with overdensities higher than eight times the overdensity threshold,  $\rho/\rho_B \geq 80$ , were refined. The following levels of refinement ( $l > 2$ ) were created refining the cells with overdensities eight times higher than their parent cells. This mechanism allows us to follow the formation and evolution of voids by forcing the numerical algorithm to numerically resolve them, and at the same time, it makes possible to have a high numerical resolution to describe the formation of all the structures within the voids.

Our simulation includes cooling and heating processes which take into account inverse Compton and free-free cooling, UV heating (Haart & Madau 1996) at  $z \sim 6$ , atomic and molecular cooling for a primordial gas, and star formation. In order to compute the abundances of each species ( $H, He, H^+, He^+, He^{++}$ ), we assume that the gas is optically thin and in ionization equilibrium, but not in thermal equilibrium (Katz, Weinberg & Hernquist 1996; Theuns et al. 1998). The tabulated cooling rates were taken from Sutherland & Dopita (1993) and they depend on the local metallicity. The cooling curve was truncated below temperatures of  $10^4 K$ . The cooling and heating were included in the energy equation (see Eq. 3 in Quilis 2004) as extra source terms.

Although the analysis of the stellar component in voids

is not considered in the present work, the description of the star formation and metallicity is introduced in the MAS-CLET code following the ideas of Yepes et al. (1997) and Springel & Hernquist (2003).

### 3 THE VOID FINDER

#### 3.1 The algorithm

Voids in simulations can be searched by looking at the regions devoid of galaxies or relying on the dark matter (and gas) distribution. The first approach has the advantage of a straightforward comparison with the observations, that can only rely on visible matter. On the other hand, using the galaxy distribution requires a good understanding of the physics of galaxy formation. As shown in several works, hydrodynamical simulations still have difficulties in reproducing the observed galaxy mass function (Crain et al. 2009), and the use of galaxies as a density tracer can lead to spurious voids. Even semi-analytical models that are designed to match the observational data as closely as possible, have shown to fail in reproducing the void distribution observed (Tavasoli, Vasei, & Mohayaee 2013). Moreover, the sparsity of the galaxy population prevents to recover the ellipticity evolution in voids (Bos et al. 2012). For all these reasons, we have built our void finder based on the continuous matter distribution. However, caution must be taken when comparing voids found with this method with observed catalogues of voids, as the two methods are based on different definitions of voids. To keep the case as general as possible we do not assume any a priori shape for the voids. This allows us to study also void morphology and its evolution with redshift. As for the density field, throughout the paper and unless otherwise specified, we consider the total density, that is the sum of the dark matter and gas components<sup>1</sup> The stellar component is not considered because its contribution to the total density in voids is negligible.

Our void finder is based on two basic assumptions: (i) voids have positive velocity divergence in the interior, with the maximum divergence being located in the void center, as a consequence of faster expansion of the inner shells with respect to the outer regions; (ii) the density at the edges has a sharp increase, hence a steep gradient. To be more precise, the algorithm performs the following steps:

(i) A grid cell is marked as candidate to be center of a void when the following both conditions are satisfied:

$$\delta < \delta_{thre} \tag{1}$$

$$\nabla \cdot \mathbf{v} > 0 \tag{2}$$

where  $\delta$  is the density contrast in a given cell,  $\delta = \rho/\rho_B - 1$ , and  $\rho$  stands for the total density, dark matter plus gas.  $\delta_{thre}$  is a free parameter and  $\mathbf{v}$  is the peculiar velocity field of the gas.

(ii) The marked cells are ranked according to the velocity divergence, from the largest to the smallest. Thus, the first void is placed around the cell with the maximum divergence.

<sup>1</sup> The continuous density field for the dark matter component is calculated by gridding the dark matter particle distribution onto the AMR grid, by means of a triangular-shaped-cloud (TSC, Hockney & Eastwood 1988) scheme.

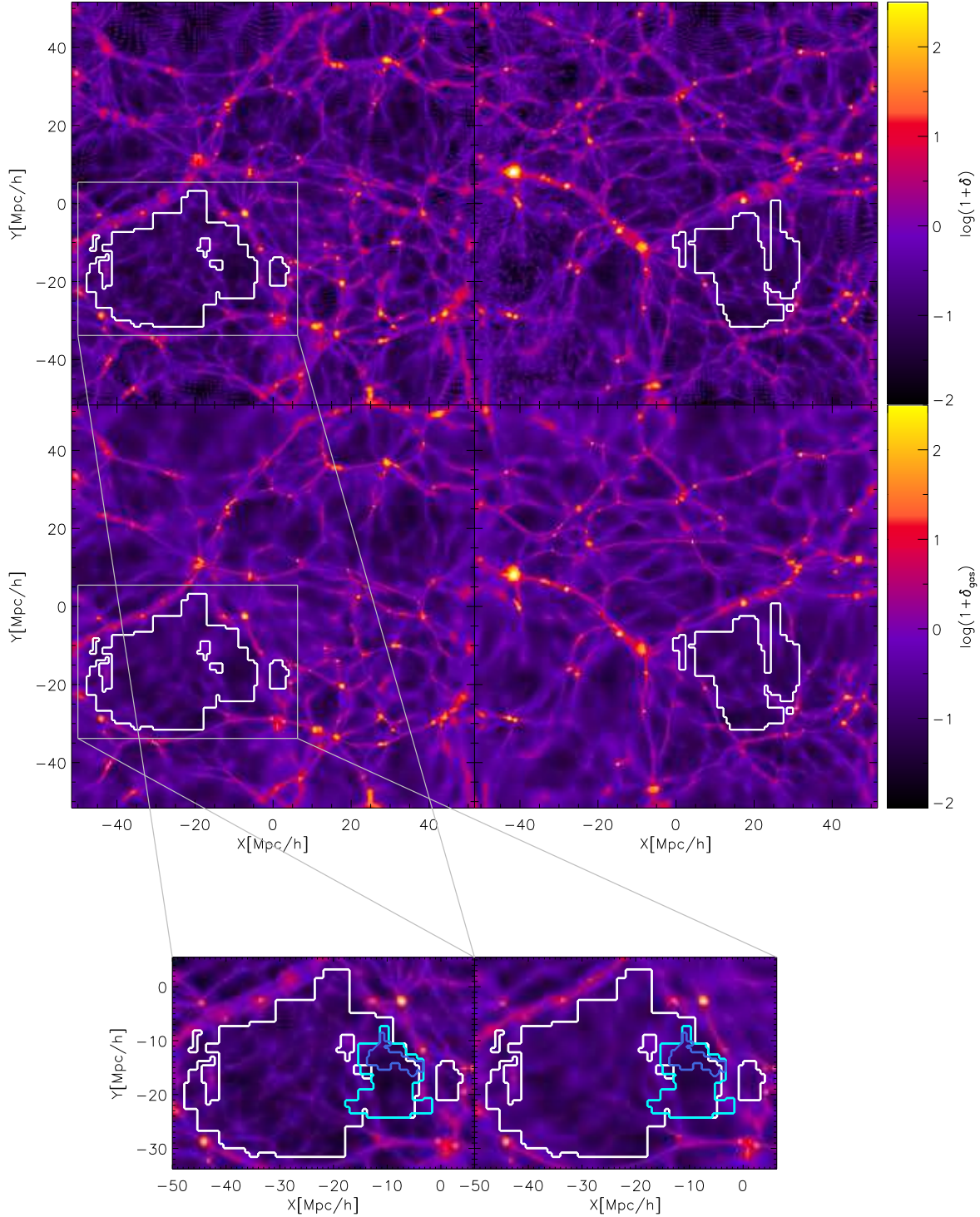


**Figure 1.** The images show the density contrast field in slices of thickness  $\sim 0.4 Mpc/h$  projected along two coordinate axes of the simulated box. In the upper panels the density contrast field includes both the dark matter and the gas components. In the lower panels we show the gas density contrast, defined as:  $(\Omega_m/\Omega_b)(\rho_{gas}/\rho_B) - 1$ . The white contours indicate the boundaries of one of the largest voids found by the void finder, having equivalent radius of  $17 Mpc/h$  and mean density contrast of  $-0.85$ . The slices are centered at the cell containing the void center. The bottom images show a zoom into the void region for the total density contrast (left) and the gas density contrast (right). Cyan and blue contours indicate voids in the middle and bottom hierarchies, respectively, contained in the parent void.

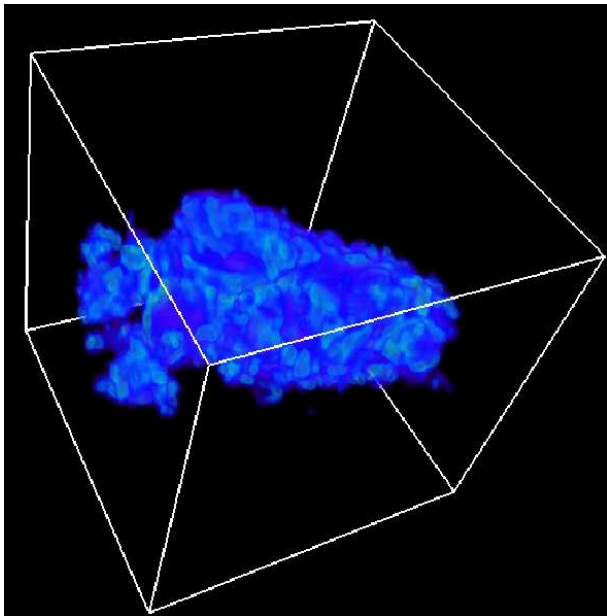


**Figure 2.** 3D representation of the same void shown in Figure 1.

(iii) The void volume is expanded by adding two cells in each coordinate direction.

(iv) The volume expansion is stopped when at least one of the following conditions applies:

$$\nabla\delta > \nabla\delta_{thre} \quad (3)$$

$$\delta > \delta_{max} \quad (4)$$

$$\nabla \cdot \mathbf{v} < 0 \quad (5)$$

where  $\nabla\delta_{thre}$  is the gradient at the void edges and  $\delta_{max}$  is the maximum density contrast allowed in a void cell. The algorithm is insensitive to this last parameter, as long as its value is large compared to the mean density in voids. We set it to  $\delta_{max} = 100$ . We have also tested the algorithm by using the velocity of the dark matter particles to compute the divergence. Given the Lagrangian nature of dark matter particles, the velocity divergence can be poorly-defined in very underdense regions when using standard methods. Since the accurate determination of the velocity divergence is crucial for the correct location of the void center, we have adopted the gas velocity approach. Alternatively, Delaunay Tessellation Field methods could be used for the velocity field reconstruction (Schaap & van de Weygaert 2000).

In this way, we find the minimum rectangle parallelepiped contained inside a void. No minimum size is set for these protovoids. Finally, we allow the protovoids to overlap with each other. When the overlapping volume is smaller than  $F_{min}$ , the two volumes are considered two separate voids, if it is larger than  $F_{max}$ , the smallest protovoid is removed from the list, whereas in the case the overlapping volume is within  $F_{min}$  and  $F_{max}$ , we merge the two protovoids, and the new center is given by the volume weighted mean of the two. The procedure is then iterated and other protovoids can merge into the same master void. At the end of the procedure, we have voids with arbitrary shape, whose volume is given by the sum of all grid volume elements contained inside the void. The void size is given by the equivalent spherical radius,  $R_e$ , i.e. the radius of the sphere which

have the same volume as the void. We describe in Section 3.3 how the free parameters involved in the procedure, namely  $\delta_{thre}$ ,  $\nabla\delta_{thre}$ ,  $F_{min}$  and  $F_{max}$ , have been chosen.

In order to take into account the hierarchical structure of voids we have run the algorithm on three grids with different resolution, so as to find the parent voids and the subvoids in two nested hierarchies. We have used the same parameter setting for each hierarchy. For the parent voids (top level of the void hierarchy) we have used the density and velocity fields smoothed on a grid coarser than the base level of the simulation, having  $128^3$  cells (spatial resolution of  $0.8 \text{ Mpc}/h$ , i.e. twice the resolution of the base level). Subvoids, i.e. voids contained in the parent voids, have been searched using the base level of the simulation ( $256^3$  cells, middle level of the void hierarchy) and the first level of refinement ( $512^3$  cells, bottom level of void hierarchy). For each subvoid level (middle and bottom hierarchies) the void finder has been applied only to the volume in voids at the previous level of hierarchy. Only voids larger than  $3 \text{ Mpc}/h$  are considered for subvoid search.

As a visual test of the goodness of the algorithm, in Figure 1 we show one of the largest voids identified in the simulation, overplotted to the density field. The visual check is very encouraging. The algorithm appears able to detect the most underdense regions in the simulated box and to correctly identify the void boundaries. We show both the total density contrast ( $\delta$ ) and the gas density contrast, defined as:  $\delta_{gas} = (\Omega_m/\Omega_b)(\rho_{gas}/\rho_B) - 1$ . Although gas dynamics is much more rich and complex than the dark matter dynamics, in low density regions, the dynamics of both components is practically identical. For an ideal gas, as the one considered in our simulation, the pressure is directly proportional to the density. In voids, the density is very low and, therefore, the pressure is extremely low as well. In this limit, the equations describing the dynamics of gas and dark matter are the same, and the evolution of both components is extremely similar. Indeed, as shown in Figure 1, the distributions of the gas density contrast and the total density contrast in void regions appear very similar.

### 3.2 Void shape

To characterize the shape of cosmic voids we fit them with an ellipsoid having the same inertia tensor as the void (Shandarin et al. 2006):

$$I_{xy} = \frac{1}{N_{cell}} \sum_{i=1}^{N_{cell}} (\delta_{xy} r_i - r_{xi} r_{yi}) \quad (6)$$

where the summation is over all the void cells  $N_{cell}$ ,  $\delta_{xy}$  is the Kronecker delta,  $r_i$  is the distance of the  $i$ -th cell to the void center and  $r_{xi}$  and  $r_{yi}$  are two components of the radial vector. To avoid to be biased toward the mass concentrations at the boundaries of voids, we assign equal weight to each void cell.

The shape of the fitting ellipsoid can be inferred from the eigenvalues of the inertia tensor:  $I_1$ ,  $I_2$ ,  $I_3$ . Thus, the semi-axes of the fitting ellipsoid can be defined as:

$$a^2 = \frac{5}{2}(I_2 + I_3 - I_1) \quad (7)$$

$$b^2 = \frac{5}{2}(I_3 + I_1 - I_2) \quad (8)$$



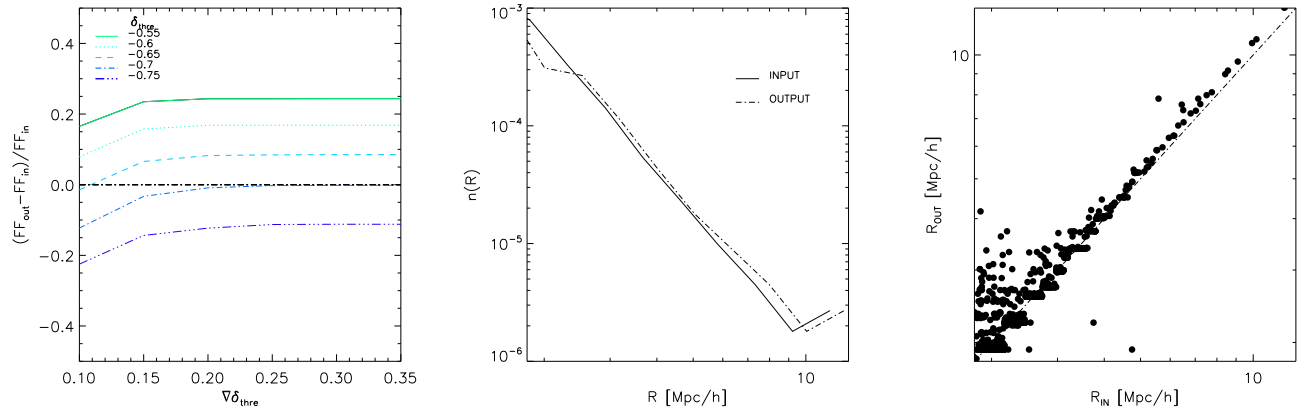


**Figure 3.** Comparison between the input catalogue of mock voids and that inferred from the void finder. The left-hand panel shows the relative difference between the obtained and the input filling fractions, as a function of the density gradient for different values of the threshold density contrast, encoded by different colours as indicated. The set of parameters giving the best match of the FF are used in the other two panels:  $\delta_{thre} = -0.7$  and  $\nabla\delta_{thre} = 0.25$ . The middle panel shows how the inferred void density function compares with the input distribution and the right-hand panel shows the comparison of void radii. Both, the density function and the recovered radii, show an excellent agreement with the input values.

$$c^2 = \frac{5}{2}(I_1 + I_2 - I_3) \quad (9)$$

where  $a \geq b \geq c$ . Finally, we can define the void ellipticity as  $\epsilon = 1 - c/a$ .

To characterize the goodness of the ellipsoidal fit we use the inverse porosity, as defined in Shandarin et al. (2006):  $IP = V_E/V$ , where  $V_E$  is the volume of the ellipsoid fitting the void and  $V$  is the actual void volume. By definition, the volume of the fitting ellipsoid is always smaller than the volume of the void, hence:  $0 \leq IP \leq 1$ . The fit can be regarded as good as much IP approaches to unity.

As shown by the three-dimensional representation of a typical void in Figure 2, voids show an irregular morphology, with level of porosity quite high and are far from being spherical.

### 3.3 Dependence on the free parameters

To prove the algorithm and test its dependence on the free parameters, we have carried out two tests. On one side, we have performed a set of Montecarlo simulations of isolated voids with realistic density profiles in order to assess the dependence of the goodness of the algorithm on  $\delta_{thre}$  and  $\nabla\delta_{thre}$ . On the other side, we have proved the performance of the algorithm when varying  $F_{min}$  and  $F_{max}$  directly on the simulations.

To assess the dependence on  $\delta_{thre}$  and  $\nabla\delta_{thre}$ , we have simulated 3000 mock voids in a  $100 h^{-1} Mpc$  box, distributed according to a power-law distribution, having size in the range:  $2-20 h^{-1} Mpc$ . The mock voids have spherical shape and are not allowed to overlap with each other. Following Colberg et al. (2005), we assume an exponential mass profile with the following form<sup>2</sup>:

$$\frac{\rho(< r)}{\rho_e} = \exp \left[ \left( \frac{r}{R_e} \right)^{1.85} - 1 \right] \quad (10)$$

<sup>2</sup> Here the Colberg profile has been slightly modified to force the density enclosed within  $R_e$  to be equal to  $\rho_e$

where  $R_e$  is the void effective radius and  $\rho_e$  is the density enclosed within  $R_e$ . We set the mean density contrast within voids to  $-0.8$ , as suggested by theoretical arguments (Sheth & van de Weygaert 2004). Outside a radius equal to  $1.2R_e$  the local density contrast is set to  $\delta_{max}$ . The velocity divergence is assumed to linearly decrease from the center to the borders. Hence, the point of maximum divergence and minimum density stays in the void center.

We have tested the algorithm by using a density contrast threshold ranging between  $-0.4$  and  $-0.8$  and a density gradient in the range  $0.1-0.4$ . In Figure 3 we compare the inferred void distribution with that of the mocks. We use the filling fraction (FF), i.e. the fraction of the volume occupied by voids, as the parameter mapping the capability of the algorithm in recovering the original distribution. For the range of parameters explored, the recovered FF differs from the input one within 20%. The algorithm is sensitive to the value chosen for the density gradient only for small gradients. For  $\nabla\delta_{thre} > 0.2$  the goodness of the void finder only depends on the density contrast threshold adopted. Density contrast thresholds within  $-0.65$  and  $-0.7$  provide the best match to the original FF (within 10%). Therefore, we choose as our fiducial values:  $\nabla\delta_{thre} = 0.25$  and  $\delta_{thre} = -0.7$ . As shown by the middle panel of Figure 3 this choice provides an excellent match to the input distribution. The recovered void radii (right-hand panel of Figure 3) also show a remarkable agreement with the input values, although a slight offset between the two is observed, mainly at small radii. The reason being that the finite size of the cells used in the void reconstruction gives volumes larger than the original spheres (the cell where the edge condition applies, see Section 3.1, is still considered as a void element). For small voids, this one-cell approximation translates into larger errors in volume and, hence, radius.

In order to assess the value of  $\nabla\delta_{thre}$  and  $\delta_{thre}$ , we have run the void finder on the mock voids, under the assumption that all the overlapping protovoids can merge to form the final void, without imposing any criterion for the overlapping volume fraction. In this case, the final void is made by all

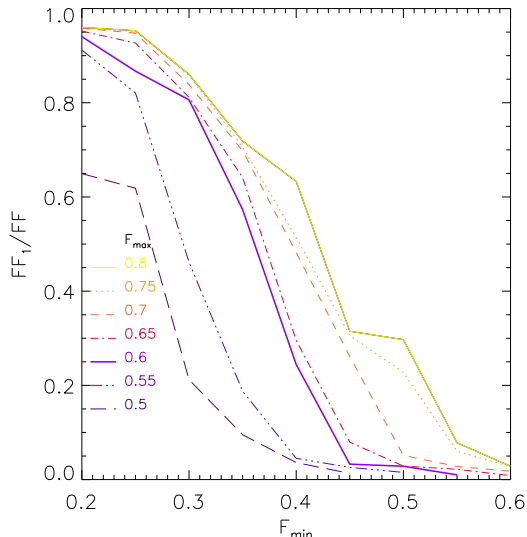


**Figure 4.** Ratio between the filling fraction in the largest void and the total filling fraction, for void catalogues obtained for different sets of  $F_{min}$  and  $F_{max}$ . The onset of percolation at low  $F_{min}$  and high  $F_{max}$  is clearly visible.

the cells satisfying the criteria for being a protovoid and the void volume can be well reconstructed. It is worth to note that such degree of accuracy in the reconstruction of the void volume can be obtained only in the idealized case of spherical, non overlapping voids. In the reality, voids have much more complex structures, and the use of too generous criteria in the overlapping fractions can lead to percolating voids. Indeed, being the void walls quite inhomogenous, the void boundaries are not always well defined and individual voids are difficult to identify. For instance, voids connected by thin tunnels would be merged together if too small values of the minimum overlapping volume were used. Therefore, beside finding the volume in voids, we require our algorithm to be able to capture the identity of individual voids.

To find the overlapping fractions providing the best solution for the real case, instead of using the mocks we have tested the algorithm directly on the simulations, using different values for  $F_{min}$  and  $F_{max}$ . In Figure 4, we show how the filling fraction of the largest void ( $FF_1$ ) found in the simulation depends on these parameters. When using too generous volume fractions (low  $F_{min}$  and high  $F_{max}$ ) for the overlapping, we see the onset of percolation. In this case the largest void, encompassing a large number of smaller voids, spans a considerable fraction of the volume in voids, filling almost the entire void volume in the most extreme cases (see red curve in Figure 4). The onset of percolation occurs quite quickly with  $F_{min}$ , while have a smoother dependence on  $F_{max}$ . For  $F_{min} > 0.45$  and  $F_{max} < 0.65$  the volume occupied by the largest void is quite stable. Therefore, we have set our fiducial values to:  $F_{min} = 0.5$  and  $F_{max} = 0.6$ .

We have checked that for small variations around the values adopted for the free parameters, the main results of this work keep unchanged.

## 4 RESULTS

### 4.1 Statistics

In this section we describe the basic statistics of the void catalogue, obtained with the fiducial values of the free parameters described in the previous section. The final catalogue at  $z=0$  includes  $\sim 600$  voids, with sizes up to  $\sim 17 h^{-1} Mpc$  and typical density contrast within the voids of  $-0.8$ . The number density of voids of a given effective radius is shown in the top-left panel of Figure 5. Voids are distributed according to a power-law distribution, with a cut-off at large radii. Hence, smaller voids are much more numerous than the larger ones. When all the voids are considered the volume in voids is 58% of the simulated volume. Since we have used a coarse grid resolution to find the parent voids, the smallest voids include only few cells, thus their structure can not be described with accuracy and the shape parameters are less reliable. Therefore, we cut our void distribution at  $3 h^{-1} Mpc$ . The filling fraction in voids above this threshold is  $\sim 0.5$ . Voids become progressively smaller in the lower hierarchies, with a maximum void radius of  $\sim 10 h^{-1} Mpc$  and  $\sim 5 h^{-1} Mpc$  for voids in the middle and bottom hierarchy, respectively.

In the top-right and bottom-left panels of Figure 5 we show the distribution for the shape parameters: inverse porosity and ellipticity. The sample of parent voids shows a significant level of porosity, with a median value of inverse porosity of  $\sim 0.55$ , implying that the void shape is very irregular and difficult to model. Similar values have been found by Shandarin et al. (2006) for voids of comparable size. It is interesting to note that voids in the lower hierarchies are less porous on average than voids located at the top of the hierarchy. The void ellipticity is shown in the bottom-left panel of Figure 5. The median ellipticity of the parent voids is 0.55, indicating that they are far from being spherical. Ellipticity also varies among the void hierarchy, with voids in the lowest level being the most spherical one ( $\langle \epsilon \rangle = 0.45$ ). Interestingly, these values are very similar to those measured in other works on void shape. Indeed, Shandarin et al. (2006) find a value of 0.55, Platen, van de Weygaert, & Jones (2008) give 0.51 and Bos et al. (2012) report 0.46. The fact we are able to reproduce the results of works that are based on completely different void finders, demonstrates the robustness of the result.

The density contrast of voids is shown in the bottom-right panel of Figure 5. The typical density contrast of the parent voids is  $-0.8$ , as expected since the algorithm have been designed to target very underdense regions (see Section 3.3). Voids in the lower levels of the hierarchy are much less dense than their parent voids. The reason being that voids in the lower hierarchies only include very thin filaments that do not contribute much to the total matter content of the void.

The redshift evolution of the void population is shown in Figure 6. As expected from theoretical arguments (Sheth & van de Weygaert 2004), we find that voids expand as time proceeds. As shown in the top-left panel of Figure 6, from high- to low-redshift the abundance of large voids increases, while at the same time, smaller voids become less numerous. Also the shape parameters display a significant evolution with redshift, as shown in the top-right

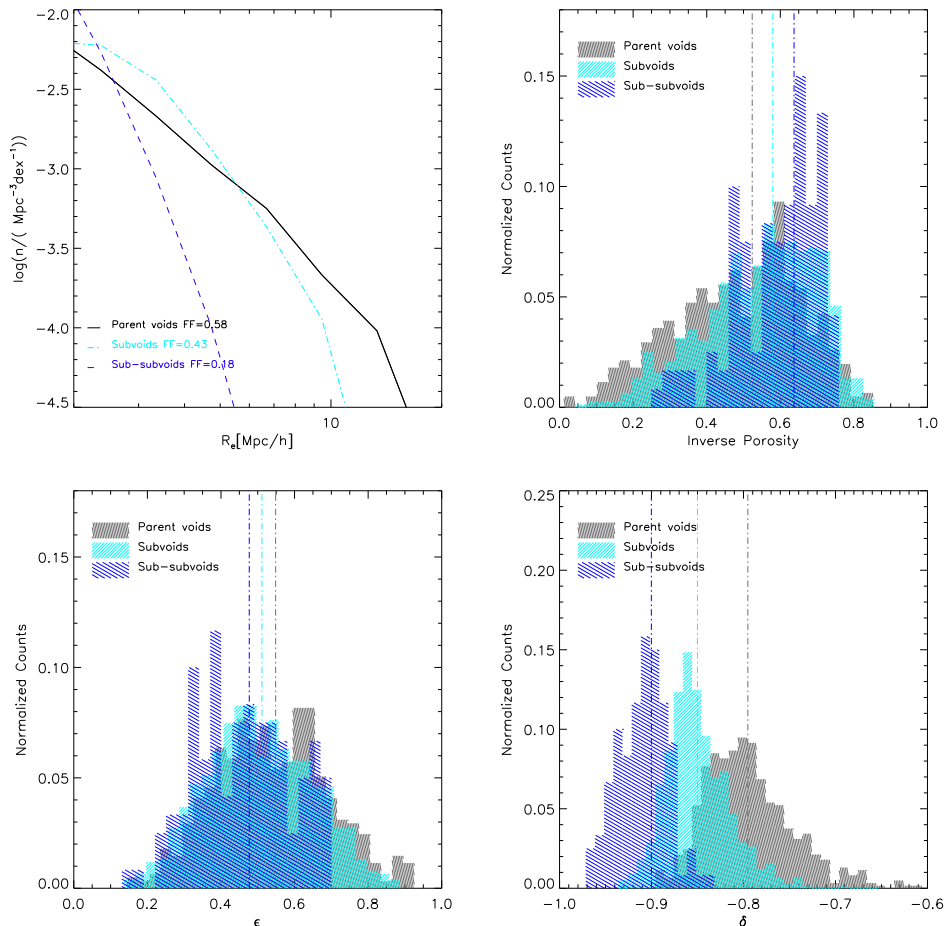


**Figure 5.** Basic statistics of the void catalogue for three void hierarchies. The top-left panel shows the number density of voids of a given effective radius. Different colours encode different levels of the hierarchy: black stays for the parent voids (top level), cyan indicates the subvoids (middle level) and blue stays for sub-subvoids (bottom level). The filling fraction of voids in each level of the hierarchy is indicated. The other three panels show the distribution of inverse porosity (top-right), ellipticity (bottom-left) and density contrast (bottom-right) for voids at the top (grey histograms), middle (cyan) and bottom (blue) level of hierarchy. Vertical lines indicate the median value of the distributions. Voids in lower levels of the hierarchy appear smaller in size, more spherical, less porous and less dense than their parent voids.

panel for the inverse porosity and in the bottom-left panel for the ellipticity. Symbols show the robust mean using a bi-weight estimator, and its standard error using all voids larger than  $3 h^{-1} Mpc$  at any given redshift. The biweight estimator (Tukey 1958) is used in order not to be affected by the presence of outliers. It belongs to the class of M-estimators, that defines the locator by the minimization of a function of the deviations of each observation from the estimate of location (see also Beers, Flynn, & Gebhardt 1990). The inverse porosity decreases with cosmic time, hence voids become increasingly more porous at low redshifts. The ellipticity shows a weak but systematic increasing as redshift decreases, evolving from  $\sim 0.53$  at  $z \sim 2.5$  up to  $\sim 0.55$  at  $z \sim 0$ . In other words, voids become more elongated as time proceeds. This appears at odds with the naive expectation according to which voids evolving in isolation become more spherical as they expand (Icke 1984; Bertschinger 1985). This would be a consequence of the anisotropic force field directed outward that induces a stronger acceleration, and hence a faster expansion, on the shortest axis direction. However, voids are

not isolated objects, and their evolution is also affected by the large scale tidal influence, to the extent that voids in realistic circumstances will never reach sphericity (Lee & Park 2009; Bos et al. 2012). Finally, the density contrast evolves considerably from a typical value of  $-0.6$  at  $z \sim 2.5$  down to  $-0.8$  at  $z \sim 0$ .

## 4.2 Density Profiles

In this section we present the density profiles for our sample of voids larger than  $3 h^{-1} Mpc$ . Because of the particular AMR implementation of this simulation, most of the void centers are located at the first level of refinement ( $l = 1$ , with spatial resolution of  $\sim 0.2 h^{-1} Mpc$ ). Hence, we compute the profiles of individual voids using the density in the AMR grid at this level. The density profiles are shown in Figure 7 for voids in the top level of the hierarchy and in Figure 8 for voids in the middle and bottom levels. The density profile is expressed in terms of enclosed density within a given radius with respect to the enclosed density within the



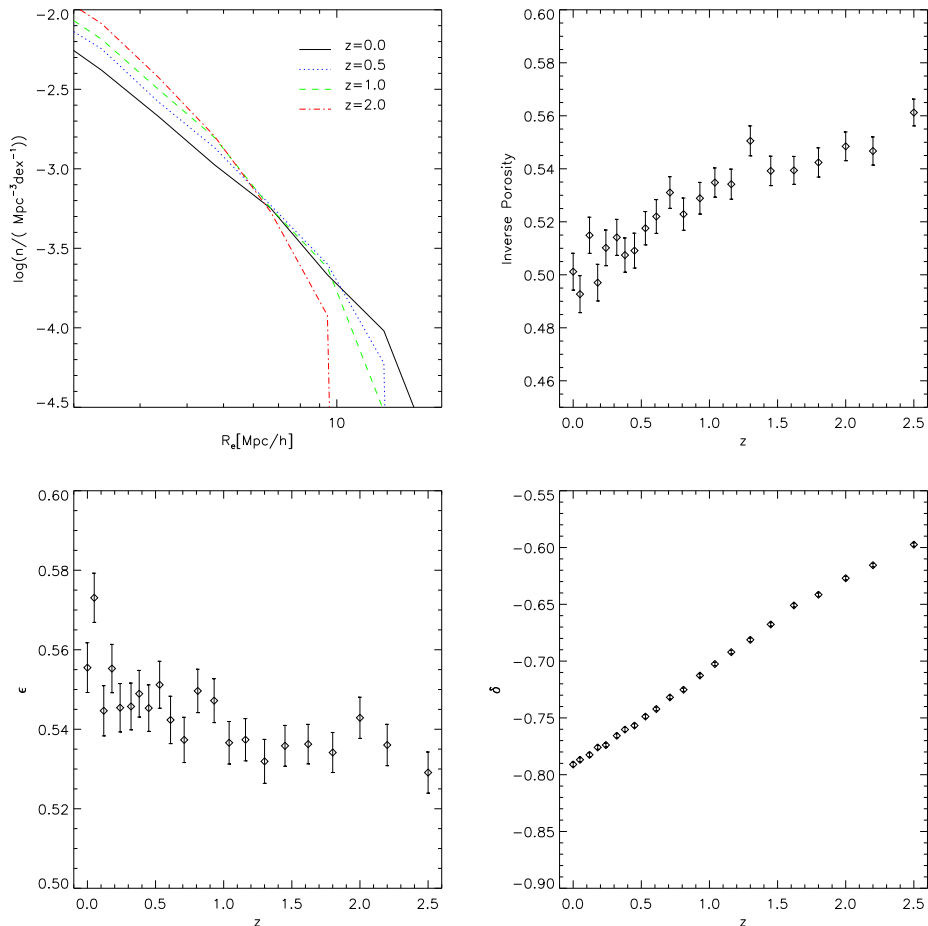


**Figure 6.** Redshift evolution of the void population. Only voids at the top level of the hierarchy and with radius larger than  $3h^{-1} Mpc$  are considered. The top-left panel shows the number density of voids for redshift ranging from 0 up to 2.5, encoded with different colours as indicated. The other panels show the redshift evolution of the mean inverse porosity (top-right panel), mean ellipticity (bottom-left) and mean density contrast (bottom-right). As cosmic time proceeds, voids become larger, more elongated and porous and less dense.

void effective radius. The individual profiles of the voids in our sample are shown as cyan lines. As shown in the previous section, typical voids are not spherical in shape. Hence, the radial apertures at large distances ( $\gtrsim R_e$ ) can include cells not belonging to the voids. Moreover, the void center may in some cases fall quite close to the boundaries and lead to bumps in the density at small radii. This can be easily seen in some of the individual profiles shown in Figure 7, where an excess of mass density is seen in the central regions (see upper curves). Therefore, our results should be interpreted as the density profiles of the regions surrounding the voids, more than the profiles of the voids themselves.

To stack the individual profiles, we rescale the radial profile of each void to its effective radius and compute a biweight estimator. To avoid edge effects we have only considered voids whose centers are more than one effective radius from the box boundaries (95% of the voids satisfy this condition). The resulting mean profile with the  $1\sigma$  confidence interval is shown in Figure 7. As a comparison, we plot also the fit of Colberg et al. (2005), measured for voids of similar sizes and given by equation (10). Our stacked profile agrees remarkably well with the exponential fit proposed by Colberg et al. (2005), although some deviations from the

Colberg profile exist. We note in passing that by adopting the same minimum void radius as in the Colberg profile ( $5h^{-1} Mpc$ ) our stacked profile does not change significantly. We have found that a better description of the void density profile is given by the following expression:

$$\frac{\rho(<r)}{\rho_e} = \left(\frac{r}{R_e}\right)^\alpha \exp\left[\left(\frac{r}{R_e}\right)^\beta - 1\right] \quad (11)$$

where  $\alpha$  and  $\beta$  are the parameters to be obtained from the fit. In Figures 7-8 the blue thick lines show the best fits. The best fit values are:  $\alpha = 0.07$  and  $\beta = 1.32$  (top level of the hierarchy, Figure 7),  $\alpha = -0.09$  and  $\beta = 0.99$  (middle level, top panel of Figure 8),  $\alpha = -0.12$  and  $\beta = 1.11$  (bottom level, bottom panel of Figure 8). Subvoids thus show much flatter profiles than their parent voids and no significant difference is observed between the density profile of voids in the middle and bottom level of the hierarchy. The steepness of the parent void profiles can be ascribed to the high density of the edges. In the case of subvoids, the steepness of the edges is limited by the condition to be contained in voids, thus high density walls are not present.

In Figure 9, we show the redshift dependence of the void radial profiles from  $z=2.5$  down to the present time. At

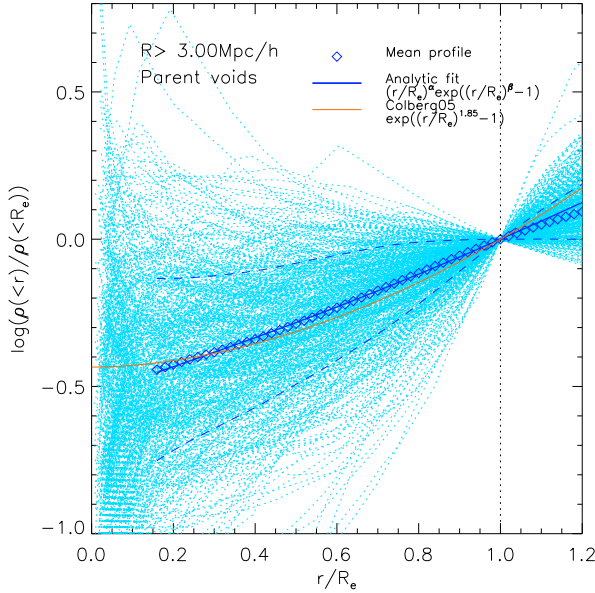


**Figure 7.** Mean density profiles for the parent voids larger than  $3 h^{-1} Mpc$ . The density profile is expressed in terms of enclosed density within a given radius with respect to the enclosed density within the void effective radius. Here and in the following figures the logarithm is base 10. The dotted cyan lines indicate the individual profiles, open symbols show the mean profile, using a biweight estimator, the thick blue line indicates the analytic fit to this profile using Eq. 11 and the blue dashed lines enclose the  $1\sigma$  confidence interval. For comparison we also show the Colberg et al. (2005) profile as orange line.

all redshifts the void sample includes only voids larger than  $3 h^{-1} Mpc$ . The void profiles become progressively steeper as time proceeds, suggesting that the interior of voids is emptying. This is in agreement with the theoretical expectations of Sheth & van de Weygaert (2004), showing the evolution of the void density profile towards a reverse top-hat shape, as a consequence of the continuous evacuation of matter from the void center. To parameterize this behavior, we show the best fit profile for each redshift in the left-hand panel of Figure 9 and the redshift dependence of the best fit parameters in the right-hand panels. A polynomial fit to the redshift dependence of  $\alpha$  and  $\beta$  is also given by:

$$\alpha = 0.08 - 0.16z + 0.03z^2 \quad (12)$$

$$\beta = 1.29 - 0.09z - 0.03z^2 \quad (13)$$

Although the evolution in the parameters is clearly visible from Figure 9, the low redshift values present a significant scatter. We ascribe this high scatter to two reasons. On one hand, at low redshift the void statistics is quite poor, as the number of small voids decreases. On the other hand, the low redshift voids are more porous than their high redshift counterparts, as shown in Figure 6, that would imply that the profiles at these redshifts are more noisy and the resulting scatter in the best fit parameters higher.

We also explore the dependence of the void profiles on the global properties of voids. In Figures 10-13, we show the profiles when the void sample is divided according to: effective radius, mean density contrast, inverse porosity and

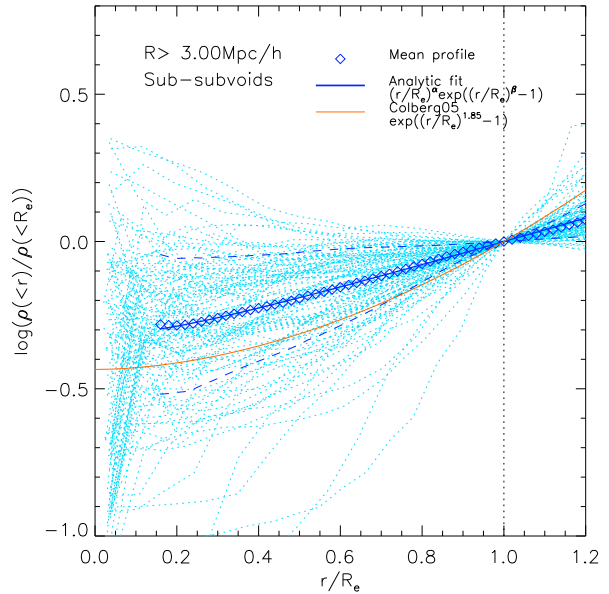
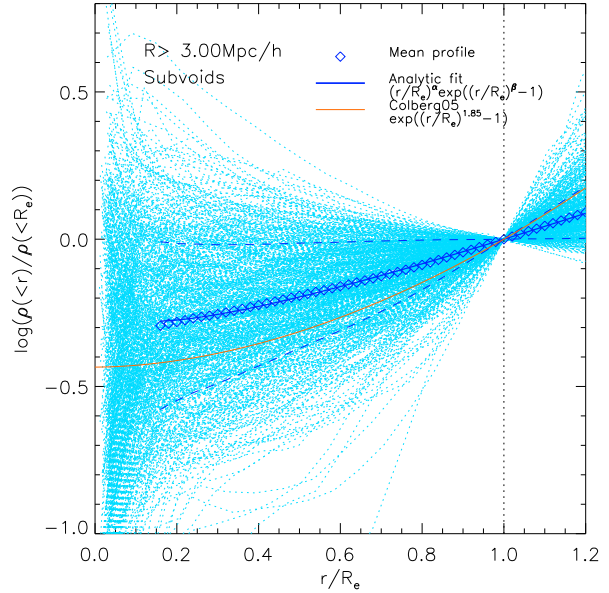


**Figure 8.** The same as Figure 7 for voids in the middle (upper panel) and bottom (bottom panel) level of the void hierarchy.

ellipticity. To enhance the statistics in each subsample we have used all voids larger than  $3 h^{-1} Mpc$  in the last five snapshots of the simulation (up to  $z = 0.25$ ). As shown in Figure 9, the variation of the free parameters  $\alpha$  and  $\beta$  in this redshift interval is quite modest, hence we do not expect to introduce any bias in the analysis due to void evolution.

The trend with radius (Figure 10) shows that the profiles are stable and the same best-fit profile applies for voids with radius up to  $R \sim 8 h^{-1} Mpc$ . Indeed, these voids can be optimally described by the same functional form used for the global population. However, there is an indication of steeper profiles in voids having higher radius (yellow and red curves). Nevertheless, as a consequence of the paucity of large voids (see Section 4.1), the statistics in the sub-samples

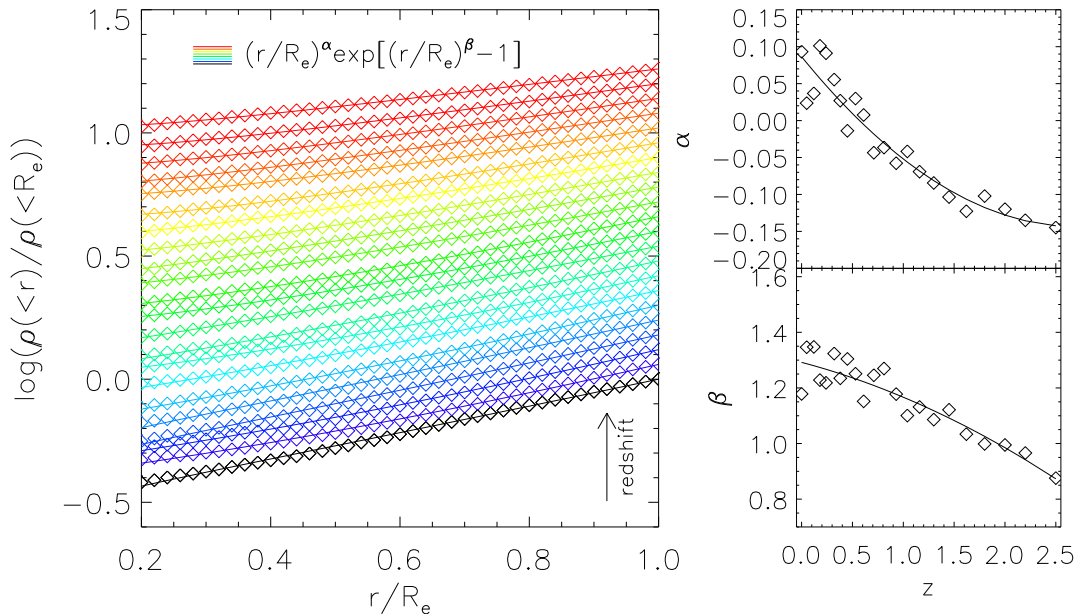


**Figure 9.** Left-hand panel: mean density profiles for voids larger than  $3h^{-1} Mpc$  at different cosmic times, with redshift increasing from the lower to the upper part of the diagram. The values of redshift can be inferred from the right-hand panels. The profiles at redshifts greater than 0 have been artificially shifted upward for the sake of clarity. Symbols indicate the void density profiles and the solid lines are fits to the density profiles using equation 11. Right-hand panels: redshift evolution of the free parameters involved in the fit, namely  $\alpha$  and  $\beta$ . The solid lines indicate a polynomial fit (see eq. 12 and 13).

with the highest radii is quite poor. Indeed, the mean profile results significantly more noisy than that of small-sized voids.

When the void sample is splitted according to the mean density contrast (Figure 11), we observe a clear separation among voids having different densities, with the least dense voids showing the steepest profile. Hence, void density appears as a much more important parameter than void radius in determining the void structure. The void profiles also show a systematic dependence on void morphology. Voids with high porosity (i.e. low inverse porosity, blue curve in Figure 12) and high ellipticity (red curve in Figure 13) show a sort of ‘bumpy’ profile, i.e. an enhanced density in the interiors, the reason being the high level of contamination in these sub-samples which leads to higher density in the interiors.

## 5 SUMMARY AND CONCLUSIONS

The simulation used in this work has been specifically designed to follow the formation and evolution of voids. It is based on an AMR scheme that, contrary to the common practice, refines the most underdense regions in the simulated volume. For the identification of voids, we have developed a numerical algorithm optimally suited to find voids in AMR simulations. Taking advantage of the AMR scheme, we have applied the procedure on different levels of refinements (which correspond to different numerical resolutions), obtaining voids on different hierarchical levels. The goodness of the void finder has been proven with the aid of a set of

mock voids having realistic profiles, showing that the algorithm is able to reproduce the input void distribution with good accuracy.

With this void finder, in a cosmological box of comoving side length  $100 Mpc/h$ , we identify  $\sim 600$  voids at redshift  $z = 0$  with sizes up to  $17 Mpc/h$  and with typical density contrast within the void region  $\delta = -0.8$ . More than half of the volume is filled by voids, with a filling fraction  $FF = 0.58$ . In agreement with previous findings, we find that voids show an irregular morphology, being quite elongated and highly porous. It is remarkable that the mean ellipticity that we find ( $\epsilon = 0.55$ ) agrees very well with that measured in other works on void shape, that use completely different void finders (Shandarin et al. 2006; Platen, van de Weygaert, & Jones 2008; Bos et al. 2012). This is a further demonstration of the reliability of the code.

Thanks to the special refinement scheme adopted, we are able to resolve the rich substructure contained within void. We have shown that subvoids appear as a rescaled version of their parent voids, having smaller sizes, lower densities and more regular morphology, being more spherical and less porous.

The morphological properties of voids show a significant evolution with redshift, with a systematic flattening of voids as time proceeds and a growing porosity. It is already known that void ellipticity should grow with time as a result of the influence of the tidal field of the large scale structure (Lee & Park 2009; Bos et al. 2012). Similarly, we interpret the growing porosity as due to the void surroundings. Indeed, if the voids were evolving in isolation, their porosity could not increase under the action of expansion only. Hence,

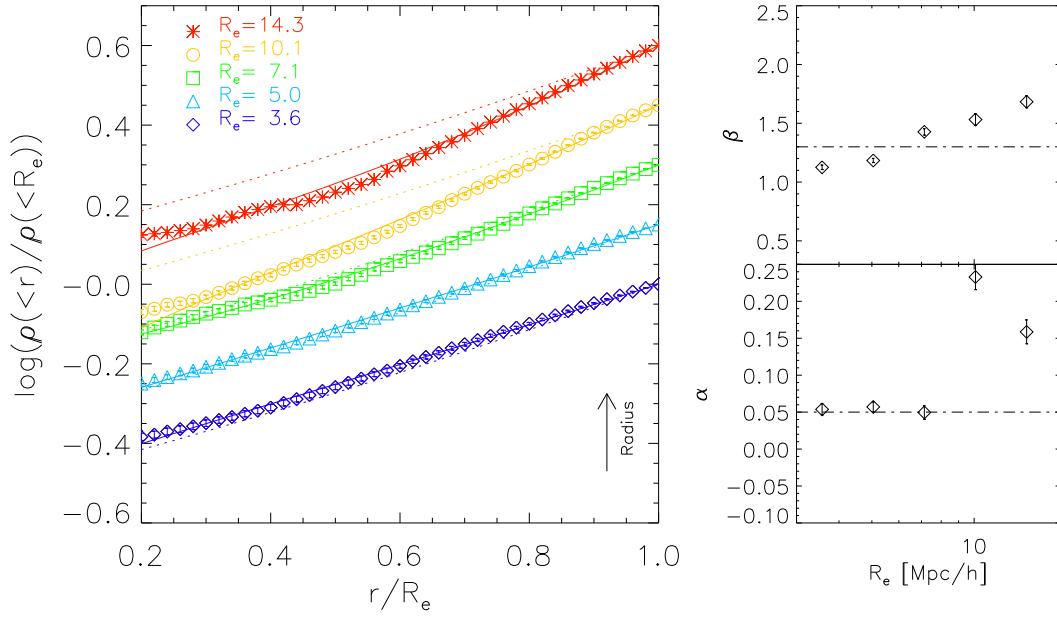


**Figure 10.** Left-hand panel: mean density profiles for voids stacked by effective radius, with radius increasing from the lower to the upper part of the diagram, as indicated. Equally spaced logarithmic bins have been used. All the profiles, except that of the subsample at the smallest radius, have been shifted upward for the sake of clearness. To enhance the statistics we have used all voids larger than  $3 h^{-1} Mpc$  in the last five snapshots of the simulation. Symbols with errorbars indicate the robust mean at each radial bin with its standard error. The solid lines indicate the best analytic fit for each subsample, whereas the dotted line is the best fit for the global population, reported for comparison. Right-hand panels: dependence of the free parameters involved in the fit ( $\alpha$  and  $\beta$ ) on the void effective radius. Errorbars indicate the formal error of the fits. The dot-dashed line indicates the values of  $\alpha$  and  $\beta$  for the global population, used for the analytic fit shown as dotted line in the left-hand panel.

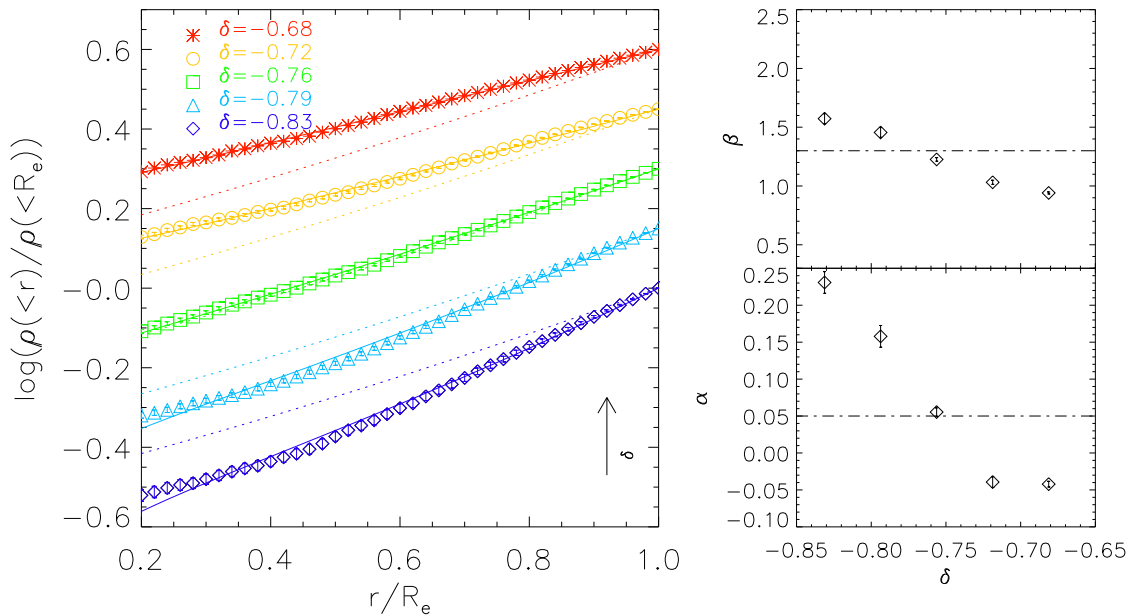


**Figure 11.** The same as Figure 10 for voids stacked according to their mean density contrast. Equally spaced bins in density contrast have been used.

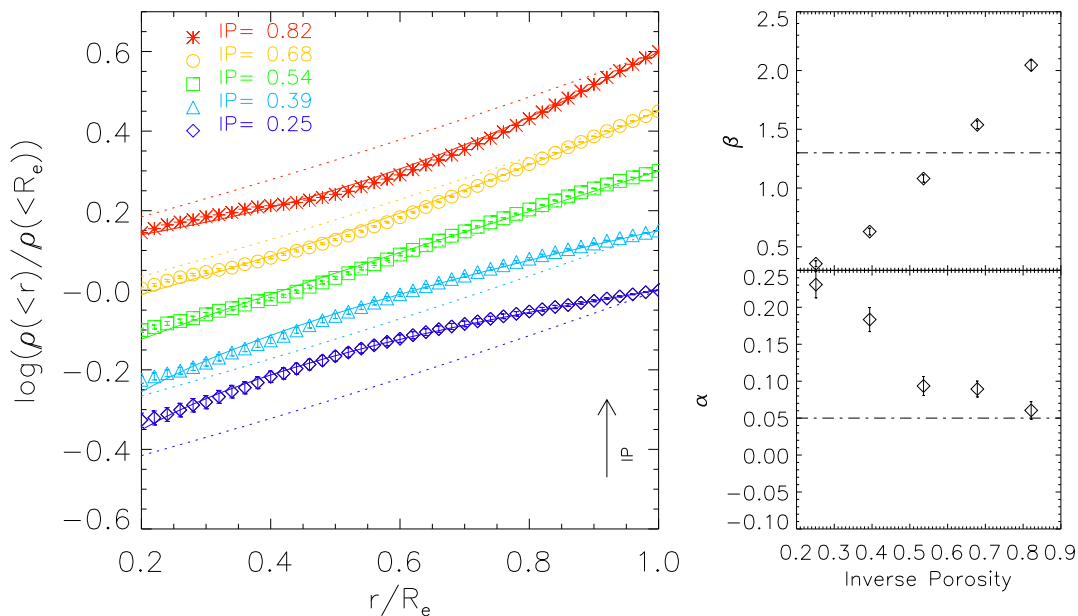


**Figure 12.** The same as Figure 10 for voids stacked according to their inverse porosity. Equally spaced bins in inverse porosity have been used.

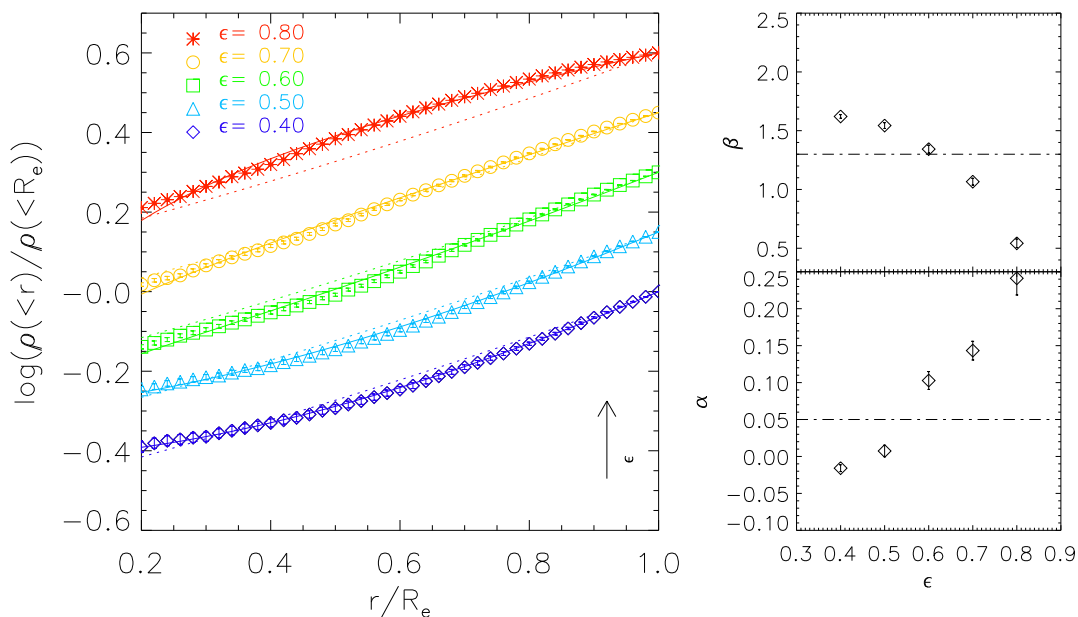


**Figure 13.** The same as Figure 10 for voids stacked according to their ellipticity. Equally spaced bins in ellipticity have been used.

we are prone to ascribe the growing porosity to void merging, that is the inclusion of small voids into the larger ones (van de Weygaert & Platen 2011).

We have also analysed the mass density profile of voids larger than  $3 Mpc/h$ , rescaled to the density enclosed within the void effective radius. To fit the void density profiles we propose a two-parameters functional form, that is a gener-

alization of the profile initially proposed by Colberg et al. (2005). We have shown that the same analytic expression can be used for voids at different hierarchical levels, though voids in the bottom levels show flatter profiles, the reason being the absence of the sharp walls present in the parent voids. The evolution of the density profile with redshift shows a progressive steepening of the profiles as cosmic time



proceeds, in agreement with the expectations from the linear theory (Sheth & van de Weygaert 2004) of an evolution towards a ‘bucket-shaped’ radial profile, as a consequence of matter evacuation.

The same functional form can also describe successfully voids having different properties. Voids of different sizes have density profiles of very similar shapes that can be fitted with the same best fit parameters. Although there is some evidence that the very large voids have a steeper profile than the global void population, the paucity of such large voids prevents us to draw robust conclusions in this respect. There is nevertheless a significant dependence of the profile steepness from the mean void density, being the least dense voids those with the steepest profile. Finally, void morphology also affects the profile, in the sense that the most porous and elongated voids display a sort of ‘bumpy’ profile, likely due to contamination from regions not belonging to the void itself.

It is worth to note that the fact that the same functional form for the void density profile can be applied to voids of any size, density, morphology and redshift suggests the existence of a universal density profile for cosmic voids, in analogy to the universal density profile for dark matter haloes.

We conclude by noticing that the particular refinement scheme adopted in this simulation is not only crucial to resolve the intricate web of void substructures, but also optimized to resolve the galaxy populations contained within voids. Although the study of void galaxies is beyond the scope of this work, we plan to address this issue in a forthcoming work.

## ACKNOWLEDGEMENTS

We would like to thank the referee for his/her suggestions that helped improving the manuscript. This work was supported by the Spanish Ministerio de Economía y Competitividad (MINECO, grants AYA2010-21322-C03-01) and the Generalitat Valenciana (grant PROMETEO-2009-103). SP also acknowledges a fellowship from the European Commission’s Framework Programme 7, through the Marie Curie Initial Training Network CosmoComp (PITN-GA-2009-238356) as well as from the PRIN-INAF09 project “Towards an Italian Network for Computational Cosmology”.

## REFERENCES

- Aragon-Calvo M. A., Szalay A. S., 2013, *MNRAS*, 428, 3409
- Beers T. C., Flynn K., Gebhardt K., 1990, *AJ*, 100, 32
- Bertschinger E., 1985, *ApJS*, 58, 1
- Bond J. R., Cole S., Efstathiou G., Kaiser N., 1991, *ApJ*, 379, 440
- Bos E. G. P., van de Weygaert R., Dolag K., Pettorino V., 2012, *MNRAS*, 426, 440
- Ceccarelli L., Padilla N. D., Valotto C., Lambas D. G., 2006, *MNRAS*, 373, 1440
- Colberg J. M., et al., 2008, *MNRAS*, 387, 933
- Colberg J. M., Sheth R. K., Diaferio A., Gao L., Yoshida N., 2005, *MNRAS*, 360, 216
- Colless M., et al., 2001, *MNRAS*, 328, 1039
- Croton D. J., et al., 2004, *MNRAS*, 352, 828
- Crain R. A., et al., 2009, *MNRAS*, 399, 1773
- Dekel A., Rees M. J., 1994, *ApJ*, 422, L1
- Eisenstein D.J., Hu W., 1998, *ApJ*, 511, 5
- Gottlöber S., Lokas E. L., Klypin A., Hoffman Y., 2003, *MNRAS*, 344, 715
- Haart F., Madau P., 1996, *ApJ*, 461, 20
- Hockney R. W., Eastwood J. W., 1988, *csup.book*,
- Hoyle B., Jimenez R., Verde L., Hotchkiss S., 2012, *JCAP*, 2, 9
- Hoyle F., Vogeley M. S., 2004, *ApJ*, 607, 751
- Icke V., 1984, *MNRAS*, 206, 1P
- Katz N., Weinberg D., Hernquist L., 1996, *ApJS*, 105, 19
- Kirshner R. P., Oemler A., Jr., Schechter P. L., Sackett P. S. A., 1981, *ApJ*, 248, L57
- Lavaux G., Wandelt B. D., 2010, *MNRAS*, 403, 1392
- Lavaux G., Wandelt B. D., 2012, *ApJ*, 754, 109
- Lee J., Park D., 2009, *ApJ*, 696, L10
- Navarro J. F., Frenk C. S., White S. D. M., 1997, *ApJ*, 490, 493
- Neyrinck M. C., 2008, *MNRAS*, 386, 2101
- Neyrinck M. C., Yang L. F., 2013, arXiv, arXiv:1305.1629
- Padilla N. D., Ceccarelli L., Lambas D. G., 2005, *MNRAS*, 363, 977
- Pan D. C., Vogeley M. S., Hoyle F., Choi Y.-Y., Park C., 2012, *MNRAS*, 421, 926
- Patiri S. G., Betancort-Rijo J. E., Prada F., Klypin A., Gottlöber S., 2006a, *MNRAS*, 369, 335
- Patiri S. G., Prada F., Holtzman J., Klypin A., Betancort-Rijo J., 2006b, *MNRAS*, 372, 1710
- Patiri S. G., Betancort-Rijo J., Prada F., 2012, *A&A*, 541, L4
- Park D., Lee J., 2007, *PhRvL*, 98, 081301
- Platen E., van de Weygaert R., Jones B. J. T., 2007, *MNRAS*, 380, 551
- Platen E., van de Weygaert R., Jones B. J. T., 2008, *MNRAS*, 387, 128
- Plionis M., Basilakos S., 2002, *MNRAS*, 330, 399
- Quilis V., 2004, *MNRAS*, 352, 1426
- Schaap W. E., van de Weygaert R., 2000, *A&A*, 363, L29
- Shandarin S., Feldman H. A., Heitmann K., Habib S., 2006, *MNRAS*, 367, 1629
- Sackett P. S. A., Landy S. D., Oemler A., Tucker D. L., Lin H., Kirshner R. P., Schechter P. L., 1996, *ApJ*, 470, 172
- Sheth R. K., van de Weygaert R., 2004, *MNRAS*, 350, 517
- Springel V., Hernquist L., 2003, *MNRAS*, 339, 289
- Sutherland R., Dopita M. S., 1993, *ApJS*, 88, 253
- Tavasoli S., Vasei K., Mohayaee R., 2013, *A&A*, 553, A15
- Theuns T., Leonard A., Efstathiou G., Pearce F. R., Thomas P. A., 1998, *MNRAS*, 301, 478
- Tukey J. W., 1958, *Ann. Math. Stat.*, 29, 614
- Yepes G., Kates R., Khokhlov A., Klypin A., 1997, *MNRAS*, 284, 235
- York D. G., et al., 2000, *AJ*, 120, 1579
- van de Weygaert R., Platen E., 2011, *IJMPS*, 1, 41
- van de Weygaert R., van Kampen E., 1993, *MNRAS*, 263, 481
- Varela J., Betancort-Rijo J., Trujillo I., Ricciardelli E., 2012, *ApJ*, 744, 82

Vogeley M. S., Geller M. J., Park C., Huchra J. P., 1994,  
AJ, 108, 745